Stress-Strain Response of a Cast 319-T6 Aluminum under Thermomechanical Loading

HUSEYIN SEHITOGLU, XINLIN QING, TRACY SMITH, HANS J. MAIER, and J.A. ALLISON

The stress-strain behavior of cast 319-T6 aluminum-copper alloys with three different secondary dendrite arm spacings (SDASs) was studied at high temperatures and under thermomechanical deformation, exposing marked cyclic softening. A two state–variable unified inelastic constitutive model proposed earlier was modified to describe the stress-strain responses of these alloys by considering the variation of hardening and recovery functions of back-stress and drag stress. The SDAS was incorporated in the model as a length-scale parameter, and the material constants were determined systematically from experiments on a cast 319-T6 aluminum with small and large SDASs. The capabilities of the constitutive model were checked by the comparisons of simulations to experiments in the small-strain regime (<0.005). The results show that the model provides successful simulations for material response after thermal exposure at high temperature and cyclic transient stress-strain behavior. The causes of mechanical behaviors at the macro scale are discussed based on microstructural changes during thermal exposure.

I. INTRODUCTION

IN recent years, cast aluminum alloys have emerged as alternative materials to cast iron and steels for automotive applications where low weight and good high-temperature performance are required. Although certain studies have been reported on the physical metallurgy and processing of cast aluminum alloys,[5–8] there are only a few studies on the mechanical behavior at high temperatures. This class of materials exhibits properties that depend strongly on local solidification conditions (often represented by secondary dendrite arm spacing (SDAS)) and heat treatment (aging treatment). To ensure the structural integrity of cast aluminum components, it is imperative to establish stress-strain models and life prediction models for these alloys. Since cast components possess a gradient of SDASs (a small SDAS in thin sections and at the surface and a large SDAS in thick sections), it is imperative to develop σ–ε prediction capabilities over a broad range of SDASs.

In the last 20 years, phenomenological constitutive modeling evolved both in the presence of time-independent and time-dependent loading cases. Initially, time-independent models based on yield-surface theory were introduced and utilized.[9,10] To account for creep effects, the classical models have been modified by adding a time-dependent creep-strain component to the time-independent plastic-strain component. This approach has the drawback of not accounting for plastic- and creep-strain interaction. More recently, unified equations have been proposed by Sehitoglu[11] that predict stress relaxation under strain holds, creep strain for stress hold, and time-dependent metallurgical changes in material structure. Time-dependent changes such as aging and recovery due to temperature holds were described for steels by Sehitoglu and co-workers.[1–4,11] Two-state variables were utilized in these constitutive models, although a single state–variable theory is also capable of representing some of the features of material response.[12] The two state–variable unified model introduced earlier[1–4,11] successfully predicted the stress-strain response of steels and Al 2080 (powder metallurgy) alloys.[13] Further modifications for the case of cast aluminum alloys, due to the unusual amount of cyclic softening and SDAS effects, are undertaken in this work. This alloy family derives its principal strength from θ' precipitates, which can coarsen and dissolve into the matrix upon exposure to high temperatures, especially under cyclic loading.

Before making attempts to develop new constitutive models, extensive experimental results on the stress-strain response of cast aluminum alloys must be obtained. In this study, the stress-strain response of Al 319-T6 alloys with different SDASs was examined under a variety of conditions. Based on these experimental observations, including thermal exposure and cyclic softening effects, the material constants were determined for Al 319-T6. The capabilities of the unified model were checked under isothermal and thermomechanical loading in the small-strain regime, for SDASs in the range from 25 to 100 μm.

II. MATERIALS AND EXPERIMENTAL PROCEDURE

A. *Material and Specimen*

The chemical composition of the cast 319-T6 aluminum-copper alloy (Al 319-T6) used in the present study is given in Table I. All specimens used for mechanical testing were prepared from a sand-cast wedge. The design of the wedge allowed machining of samples with a predetermined SDAS. The cooling rate during solidification affects the dendrite arm spacing, porosity level, and morphology of the intermetallic phases present.[14] The average area porosity levels

HUSEYIN SEHITOGLU, Professor, and TRACY SMITH, Graduate Research Assistant, are with the Department of Mechanical and Industrial Engineering, University of Illinois, Urbana, IL 61801. XINLIN QING, formerly Postdoctoral Research Scientist, Department of Mechanical and Industrial Engineering, University of Illinois, is Postdoctoral Fellow, Aeronautical and Astranautical Engineering Department, Stanford University, Palo Alto, CA 94305. HANS J. MAIER, Professor, formerly with the University of GH Siegen, Siegen, Germany, is with University of GH Paderborn, Paderborn 33098, Germany. J.A. ALLISON, Senior Staff Technical Specialist, is with the Ford Research Laboratory, Dearborn, MI 48121.

Manuscript submitted May 12, 1998.

Table I. Material Composition in Weight Percent

Element	Si	Cu	Mg	Fe	Mn	Zn	Ti	Cr	Sr	Al
Wt (pct)	7.43 ± 0.34	3.33 ± 0.16	0.22 ± 0.03	0.38 ± 0.04	0.24 ± 0.02	<0.25	0.12 ± 0.02	<0.05	0.03 ± 0.01	bal

were 0.04 pct for small, 0.87 pct for medium, and 2.02 pct for large SDAS cases, respectively. Specimens from the tip of the wedge have the small SDAS (25 μm), those from the midsection have the medium SDAS (55 μm), and those specimens far away from the tip possess the large SDAS (100 μm). Figures 1(a) and (b) show that, depending on the cooling rate during solidification, the microstructures appear quite different. Figure 1(a) depicts the microstructure for a small SDAS, and Figure 1(b) shows that for a large SDAS. In the present study, experiments were performed on both of these materials in addition to the intermediate (70 μm) SDAS material. After solidification through the use of a copper chill at the tip of the wedge, the wedges were cooled to room temperature (RT). Then, the cast material was heat treated with a solution treatment for 8 hours at 495 °C, followed by a boiling-water quench and peak aging of 5 hours at 190 °C. The material was then given a T6 heat treatment (5 h/190 °C) to achieve a peak-aged condition. A series of aging treatments and hardness measurements were made before the selection of this peak-aged treatment. Samples were cut from three sections of the wedge; those samples with a small SDAS had a range of SDASs between 25 and 35 μm, and those samples with a large SDAS had a range of SDASs between 85 and 120 μm. Transmission electron microscopy (TEM) techniques were used to study the microstructure of the cast aluminum alloy.

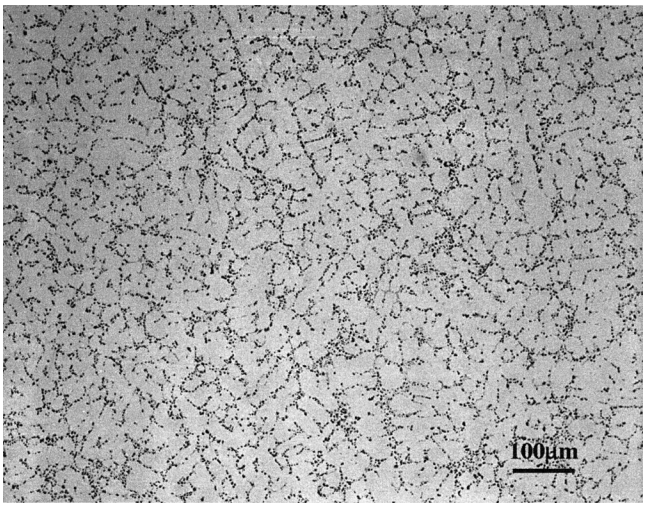

(*a*)

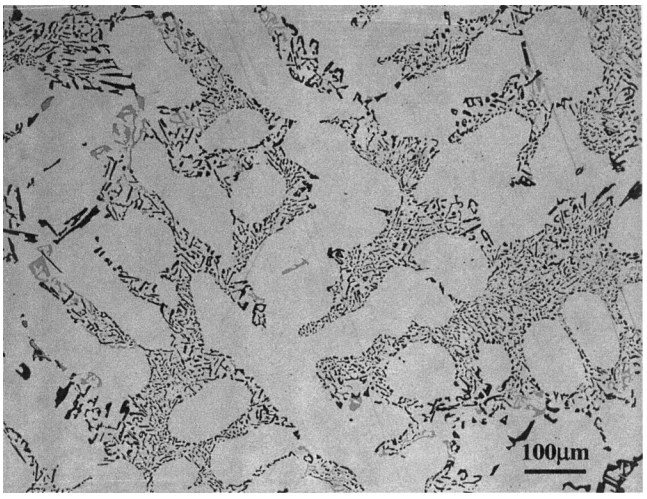

(*b*)

Fig. 1—(*a*) Micrograph showing Al319-T6 with SDAS for T6 small SDAS (~30 μm). (*b*) Micrograph showing Al319-T6 with SDAS T6 large SDAS (~90 μm).

B. *Experimental Details*

A servohydraulic MTS test machine with computer control was used in thermomechanical loading cases. The computer control unit was capable of handling load/strain/temperature control. The temperature control is within 3 °C, and the load/strain control is within the ASTM standards. An induction heating unit (Lepel, 15 kW) was used for heating the specimen. No forced cooling was used to avoid thermal gradients. Strain was measured using an MTS high-temperature extensometer with a 25.4-mm gage length. The specimens were dog bone–shaped, with a gage length of 25.4 mm and a diameter of 7.62 mm. Isothermal fatigue tests in the low-cycle fatigue regime were conducted at strain rates ranging from 5×10^{-5} s^{-1} to 1×10^{-2} s^{-1} at 20 °C and 250 °C. At RT, the material does not exhibit strain-rate sensitivity. The strain rate of 5×10^{-5} s^{-1} was selected for the high-temperature experiments, because it corresponds to the strain rate in the thermomechanical fatigue (TMF) experiments. When the stress-strain model is developed, it is important to test the model under conditions where both temperature and strain are varied. The TMF experiments fullfill this role. The maximum temperature in the TMF experiments was 300 °C, and the minimum temperature was 100 °C. Out-of-phase (OP) conditions were studied, where the maximum temperature coincides with the minimum strain at a constant mechanical strain rate of 5×10^{-5} s^{-1}. Tests began at 200 °C at zero stress and zero mechanical strain. As the temperature is increased, the specimen undergoes compression first, which is followed by cooling to 100 °C, where tensile stresses develop. The temperature variation along the gage length of the specimen was as low as ± 3 °C, and the temperature control was also within 3 °C. This was achieved by optimizing the induction coil design. Consequently, no barreling of the specimens was observed. Both the temperature and mechanical-strain waveforms were triangular, with no hold periods. The mean mechanical strain is zero, but tensile mean stresses develop due to the asymmetry of the cycle. More details on the experimental techniques can be found in References 4 and 11.

Creep experiments were conducted at the Ford Research Laboratory, at constant load and at temperatures ranging from 150 °C to 250 °C. These experiments were completed

on Al 319-T6 alloys with small, medium, and large SDASs. A series of tensile experiments at RT were also performed after thermal exposure at 100 °C, 180 °C, and 250 °C for exposure times in the range from 1 to 1000 hours, respectively. The thermal-exposure experiments were conducted at Ford Research Laboratory by Reeber.[21]

III. UNIFIED CONSTITUTIVE MODEL AND STATE VARIABLES

The two state–variable unified constitutive model basically proposed earlier[1–4,11,13] has been modified to describe the stress-strain behavior of high-temperature cast aluminum alloys. The functional form of the flow rule is given as

$$\dot{\varepsilon}_{ij}^{in} = A\, f\left(\frac{\overline{\sigma}}{K}\right) \frac{S_{ij} - S_{ij}^{C}}{\overline{\sigma}} \qquad [1]$$

where $\dot{\varepsilon}_{ij}^{in}$ represents the inelastic strain rate; K is the drag stress, which represents the size of the stress surface; S_{ij} is the deviatoric stress, S_{ij}^{C} is the deviatoric internal (back) stress; and $\overline{\sigma}$ is the effective stress, defined as $\overline{\sigma} = (3/2\,(S_{ij} - S_{ij}^{C})(S_{ij} - S_{ij}^{C}))^{1/2}$. The term $S_{ij} - S_{ij}^{C}$ describes the direction of the inelastic strain rate. The term $f\,(\overline{\sigma}/K)$ is a scalar function and depends on the operative mechanism, such as power-law creep, plasticity, and diffusion flow. The form of the flow rule, given as Eq. [1], is established from yield-strength measurements at different temperatures and strain rates. The constant A is a function of temperature and SDAS and can be expressed as follows:

$$A = A_c \left(\frac{L}{L_0}\right)^{m_0} \exp\left(-\frac{\Delta H_c}{\mathrm{R}T}\right) \qquad [2]$$

where L is the size of the SDAS, L_0 is a normalization distance, and the coefficient A_c and the exponent m_0 are constants.

There are two state variables in this model: the back-stress and the drag stress. The back-stress describes the directional (internal) stress fields due to dislocation pileup at precipitates, grain boundaries, and other obstacles. Its sign varies during the cycle. The drag stress is introduced to characterize the material-strength dislocation density and dislocation morphology (such as cell size) and precipitate-spacing effects. It is a positive, scalar quantity that varies gradually with the number of cycles and over time. The two state variables evolve throughout the deformation history in a recovery-hardening format, as

$$\dot{S}_{ij}^{C} = \frac{2}{3} h_\alpha(\overline{\alpha}, L)\dot{\varepsilon}_{ij}^{in} - (r_\alpha^D(\overline{\alpha}, T, \overline{\varepsilon}^{in}, L)\dot{\overline{\varepsilon}}^{in} + r_\alpha^s(\overline{\alpha}, T, L))S_{ij}^{C}\dot{} \qquad [3]$$

$$\dot{K} = h_k(K, T, L)\dot{} - r_k(K, T, L) + \theta(K, T, L)\dot{T} \qquad [4]$$

In Eqs. [3] and [4], $\dot{S}_{ij}^{C}$ is the deviatoric back-stress rate, $\dot{K}$ is the drag-stress rate, θ represents the variation of K_0 (initial value of drag stress measured on a specimen which has undergone the T6 treatment) with temperature (T) as $\partial K_0/\partial T$, $\dot{T}$ is the temperature rate, h_α and h_k are the hardening functions, r_α^D and r_α^s are the dynamic and static recovery functions for the back stress, respectively, and r_k is the recovery function for drag stress. The term $\overline{\alpha}$ is the effective back-stress, defined as $\overline{\alpha} = \sqrt{3/2 S_{ij}^{C} S_{ij}^{C}}$. The functions f($\overline{\sigma}/K$), h_α, h_k, r_α^D, r_α^s, r_k and θ are determined directly from the experiments. Unlike previous forms with no length parameter, the SDAS(L) has been explicitly incorporated into the hardening functions and recovery terms.

The previous equations are written in three-dimensional form, but it is relatively simple to specialize them for the uniaxial case. If the applied stress is denoted by σ and the inelastic strain is denoted by ε^{in}, then $S_{11} = 2/3\,\sigma$, $S_{22} = S_{33} = -1/3\,\sigma$, $S_{11}^{c} = 2/3\,\alpha$, $S_{22}^{c} = S_{33}^{c} = -1/3\,\alpha$, and $\varepsilon_{11} = \varepsilon^{in}$ and $\varepsilon_{22} = \varepsilon_{33} = -1/2\,\varepsilon^{\mathrm{in}}$.

A. *Determination of the Flow Rule*

The flow rule describes the inelastic strain rate as a function of the material internal state. It reflects different deformation mechanisms that lead to different strain-rate-sensitivity regimes. To determine the flow rule, creep experiments, monotonic tensile experiments, and isothermal fatigue experiments were utilized. From these experiments, the initial yield stress at a very small strain offset (0.005 pct) was determined for different inelastic strain rates and temperatures. This very small offset was intentionally chosen in order to capture the small-strain deformation regime.

Before the σ-ε^{in} response is established, the elastic modulus ($E(T)$) must be determined. For these materials, the elastic modulus was determined to be E(T) = 77,000 − 53 T (°C) MPa from a series of monotonic experiments, and the inelastic strain at any point in the cycle (for an isothermal experiment) was calculated to be

$$\varepsilon^{in} = \varepsilon^{\mathrm{total}} - \frac{\sigma}{E} \qquad [5]$$

where E is the elastic modulus, σ is the current stress, and $\varepsilon^{\mathrm{total}}$ is the mechanical strain. The experimental stress *vs* inelastic strain is shown in Figure 2. The 0.005 pct offset yield stress is obtained accurately from Figure 2 at different temperatures, because the strain resolution is below this

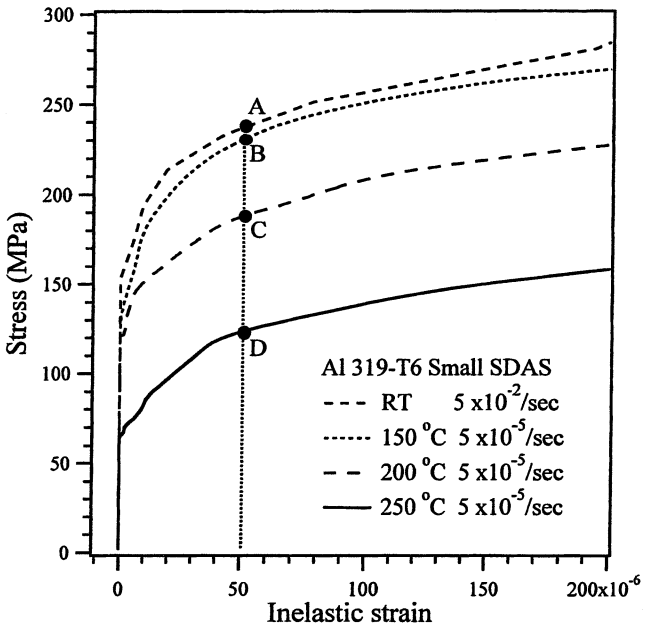

Fig. 2—Determination of yield stress at 0.005 pct strain offset (A, D).

offset value. The letters A, B, C, and D in Figure 2 correspond to offset yield stress at RT, 150 °C, 200 °C, and 250 °C, respectively. We note the nearly two-fold decrease in flow stress as the temperature is raised from RT to 250 °C. Also, note that there is no strain-rate sensitivity observed at RT in this class of materials.

When the inelastic strain rate is plotted *vs* the yield stress, it is possible to establish the flow rule (Eq. [1]) for this material. Two mechanisms are seen: power-law creep and plasticity (Figure 3). The initial drag stress is defined by the yield stress at the intersection of the power-law creep and plasticity mechanism at 250 °C. This is shown by the vertical line in Figure 3. At other temperatures, K_0 is determined by setting $K_0/E(T)$ to be constant.[2,3] The inelastic strain rate and the yield stress are normalized by $A(T)$ and K_0, respectively. The parameter $A(T)$ is related to the activation energy of the deformation and applies to the entire temperature range studied. The plots of normalized inelastic strain rate *vs* $\bar{\sigma}/K$ for Al 319-T6 samples with small and large SDAs are shown in Figures 3 and 4, respectively. The data points were obtained from experiments under a variety of temperatures, strain rates, and conditions, as described in the legends. The temperature and SDAS dependencies of A, K_0, and E are given in Table II. The flow rule, which relates the inelastic strain rate to the state variables, is established from Figures 3 and 4 as

$$\frac{\dot{\varepsilon}_{ij}^{in}}{A} = \begin{cases} \left(\frac{\bar{\sigma}}{K}\right)^{n_1} \frac{S_{ij} - S_{ij}^C}{\bar{\sigma}} & \left(\frac{\bar{\sigma}}{K}\right) < 1 \\ \exp\left(\left(\frac{\bar{\sigma}}{K}\right)^{n_2} - 1\right) \frac{S_{ij} - S_{ij}^C}{\bar{\sigma}} & \left(\frac{\bar{\sigma}}{K}\right) \geq 1 \end{cases} \quad [6]$$

where n_1 and n_2 are constants, and the coefficient A is a temperature-dependent term. The experimentally determined value of n_1 is 6.0 for both materials with small and large SDASs. This value is obtained consistently for all the materials studied, independent of the SDAS. The coefficient A depends on the SDAS *via* the exponent (Table II) m_0, which is close to 1. This means that, at a constant value of $\bar{\sigma}/K$, the plastic flow increases linearly with the increasing length of the SDAS. The first part of the equation (power-law form) describes the power-law creep regime, while the second part (exponential form) describes the plasticity regime. The solid line in Figures 3 and 4 is obtained based on the correlation given in Eq. [6]. When $\bar{\sigma}/K \geq 1$, the response is in the plasticity domain. The value of the exponent n_2 is 13, which corresponds to the steep slope in the

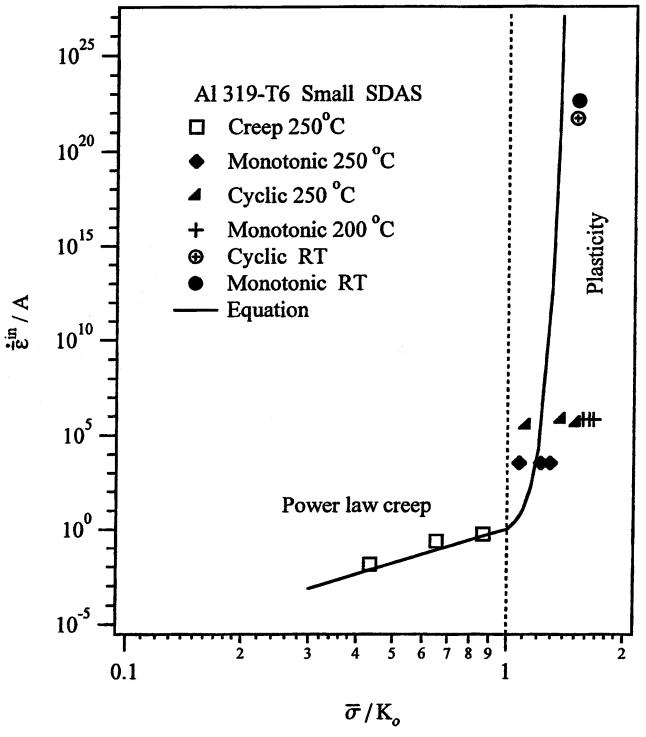

Fig. 3—Determination of flow rule for Al 319-T6 small SDAS through (14 tests).

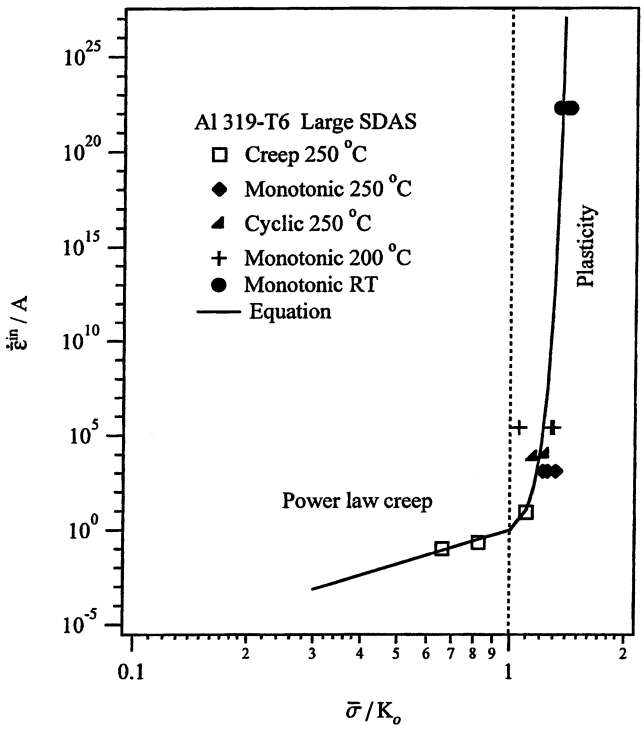

Fig. 4—Determination of flow rule for Al 319-T6 large SDAS (14 tests).

Table II. Summary of Flow Rule for Al 319-T6

$$\frac{\dot{\varepsilon}_{ij}^{in}}{A} = \begin{cases} \left(\frac{\bar{\sigma}}{K}\right)^{n_1} \frac{S_{ij} - S_{ij}^C}{\bar{\sigma}} & \left(\frac{\bar{\sigma}}{K}\right) < 1 \\ \exp\left[\left(\frac{\bar{\sigma}}{K}\right)^{n_2} - 1\right] \frac{S_{ij} - S_{ij}^C}{\bar{\sigma}} & \left(\frac{\bar{\sigma}}{K}\right) \geq 1 \end{cases}$$

$$A = A_c \left(\frac{L}{L_0}\right)^{m_0} \exp\left[-\frac{\Delta H_c}{RT}\right]$$

$$E = 77{,}000 - 53.0T\ (°C)\ (MPa)$$

$$K_0 = K_1 \left(\frac{L}{L_0}\right)^{m_1} - K_2 \left(\frac{L}{L_0}\right)^{m_1} T\ (°C)$$

$K_1 = 109$ MPa $K_2 = 0.076$ MPa/° C
$A_c = 6.24 \times 10^{13}\ s^{-1}$, $\Delta H_c = 213.7$ KJ/mol,
$n_1 = 6.0$, $n_2 = 13.0$, $m_0 = 0.88$, $m_1 = -0.214$, $L_0 = 60\ \mu m$

$$\dot{\varepsilon}_{ij}^{total} = \dot{\varepsilon}_{ij}^{e} + \dot{\varepsilon}_{ij}^{in} + \dot{\varepsilon}_{ij}^{th}$$

$$\dot{\varepsilon}_{ij}^{e} = \{(1-\nu)\dot{\sigma}_{ij} - \nu\dot{\sigma}_{kk}\,\delta_{ij}\}/E - \{(1-\nu)\sigma_{ij} - \nu\sigma_{kk}\,\delta_{ij}\}\frac{\partial E}{\partial T}\frac{\dot{T}}{E^2}$$

plasticity regime of Figures 3 and 4. We note that some inherent scatter in the data exists in this class of materials, because the specimens were cut from castings, and the presence of porosities is inevitable.

As listed in Table II, the dependence of stress exponents and elastic modulus on SDAS is negligible, but the initial drag stress depends strongly on SDAS and decreases with increasing SDAS. It is interesting to note that since $m_1 = 0.214$, K_0 varies as $L^{-1/5}$. We also note the total-strain-rate equation in Table II, which is the sum of the inelastic, elastic, and thermal components of strain. The elastic strain rate is defined in the last row of Table II, where v represents Poisson's ratio and δ_{ij} is the Kronecker delta. The thermal strain rate (ε_{ij}^{th}) is the product of the coefficient of thermal expansion and temperature rate.

B. *Hardening and Recovery Functions of Back-Stress*

From unidirectional straining such as a monotonic test conducted at high strain rates and low temperatures, the effective back-stress can be measured approximately as the current stress minus the material-yield stress (σ-σ_{ys}). The determination of the back-stress hardening term (h_α) can be achieved at RT, since, in this class of alloys, recovery is negligible at RT. In this article, a uniaxial stress–inelastic strain reversal from the first cycle was used to determine the back-stress hardening coefficients. As shown in Figure 5, we select M points in the $\Delta\sigma$–$\Delta\varepsilon^p$ curve (the backbone of the hysteresis loop) from the cyclic experiment where the uniaxial loading begins from the most compressive stress state.[10] The slope of this curve at every point (i) is determined and plotted in Figure 6(a). The horizontal axis is the effective back-stress, defined as σ-σ_{ys} and the slope is h_α. The function $h_\alpha = a_1 \exp(-(a_2\overline{\alpha})^{a_3})$ is a fine fit for the data where $\overline{\alpha}$ is the effective back-stress, defined earlier. In Figure 6(a), we note that h_α/E is highest for the small SDAS and lowest for the material exposed to high temperatures. In this case, after thermal exposure at 250 °C for 1000 hours, the specimen was tested at RT. The magnitude of the back-stress

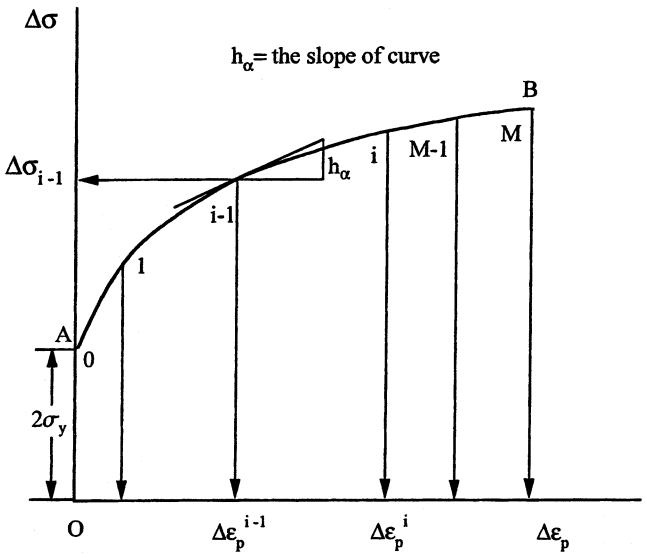

Fig. 5—Illustration of the procedure to determine h_α from a uniaxial stress–inelastic strain reversal.

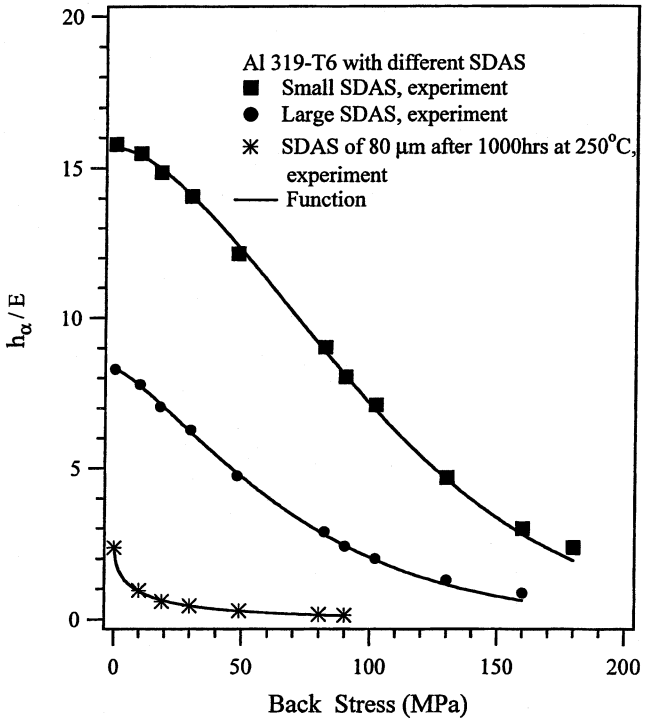

(*a*)

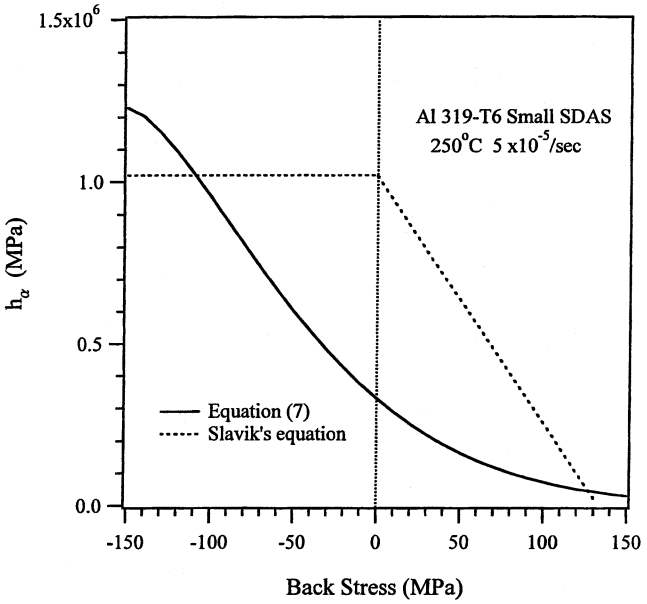

(*b*)

Fig. 6—(*a*) Back-stress hardening function for Al 319-T6 from a uniaxial stress–inelastic strain reversal. (*b*) The comparison of different hardening functions of back-stress for uniaxial reversal when $\varepsilon > 0.0$.

hardening term (star data points) is nearly tenfold lower than in the case of the unexposed specimen.

For cyclic loading, the following modification is made to h_α. The magnitude of back-stress at the most compressive stress is a minimum and, upon straining in the tensile direction, the magnitude of back-stress first reaches zero and then becomes positive. The constant α_0 is introduced into the h_α term to describe the limiting value of the back-stress. As shown in Figure 6(b), Eq. [7] describes the hardening term

in the back-stress-rate expression more accurately than the expression used earlier.[2,3] Upon selection of the constant α_0, the variation of h_α upon unloading (solid line) is smooth, as opposed to the discontinuous slope in the original Slavik–Sehitoglu model. Then, the back-stress hardening term h_α for Al 319-T6 could be described by the following equations:

$$h_\alpha(\alpha, L) = \begin{cases} a_1 \exp(-(a_2(\alpha_0 + \overline{\alpha}))^{a_3}) & \text{if } \dot{\varepsilon}^{in} \cdot \alpha \geq 0 \\ a_1 \exp(-(a_2(\alpha_0 - \overline{\alpha}))^{a_3}) & \text{if } \dot{\varepsilon}^{in} \cdot \alpha \leq 0 \end{cases} \quad [7]$$

The coefficients a_1, a_2, and a_3 are assumed to be a function of SDAS as

$$a_1 = a_{10}\left(\frac{L}{L_0}\right)^{m_2}, \quad a_2 = a_{20}\left(\frac{L}{L_0}\right)^{m_3}, \quad a_3 = a_{30}\left(\frac{L}{L_0}\right)^{m_4} \quad [7a]$$

where a_{10}, a_{20}, a_{30}, m_2, m_3, and m_4 are six back-stress hardening coefficients and exponents, respectively. From the material response after thermal exposure (Figure 6(a)), it is found that the back-stress hardening function is time dependent due to the metallurgical changes of the material structure. The coefficients a_1, a_2, and a_3 are functions of time and temperature. The coefficients decrease as the saturated values ($a_{i\text{sat}}$, i being equal to 1, 2, or 3) are approached. We assume that the variation rates of the back-stress hardening coefficient could be expressed as follows:

$$\dot{a}_i = -c_i(a_i - a_{i\text{sat}}) \exp\left(-\frac{\Delta H_i}{RT}\right) \quad (i = 1, 2, \text{ or } 3) \quad [8]$$

where $a_{i\text{sat}}$ (i = 1, 2, or 3) are the saturated values of a_1, and a_2, and a_3, respectively, after 1000 hours at 250 °C. The constants $a_{i\text{sat}}$, c_i, ΔH_i (i = 1, 2, or 3) were determined from monotonic tensile experiments performed at RT after the materials had been thermally exposed at 180 °C for 300 and 1000 hours and at 250 °C for 300 and 1000 hours. The constants in Eq. [7] and [7a] are listed in Table III.

The back-stress recovery term can be determined from experiments performed at high temperatures. In the present study, based on the experimental evidence, we assume the static recovery term of the back-stress to be small ($r^s_\alpha(\alpha, T, L) \cong 0$) and dynamic recovery from r^D_α to be dominant. In the uniaxial case, Eq. [3] can be written as follows:

$$\dot{\alpha} = h_\alpha(\alpha, L)\dot{\varepsilon}^{in} - r^D_\alpha(\alpha, T, \dot{\overline{\varepsilon}}^{in}, L)\dot{\alpha}\dot{\overline{\varepsilon}}^{in}$$

Then, upon rearranging,

$$r^D_\alpha(\alpha, T, \dot{\overline{\varepsilon}}^{in}, L) = \frac{\left(h_\alpha(\alpha, L) - \frac{d\alpha}{d\varepsilon^{in}}\right)}{\alpha} \quad [9]$$

where $d\alpha/d\varepsilon^{in}$ is the slope of the back-stress vs inelastic-strain curve. Either the monotonic or the first reversal of the cyclic experiments, performed at 250 °C and 150 °C, may be used to determine the back-stress recovery term (they yield the same result). The results reveal that the back-tress recovery term can be expressed as a function of the back-stress and the inelastic strain rate as

$$r^D_\alpha(\overline{\alpha}, T, \dot{\overline{\varepsilon}}^{in}, L) = c(\overline{\alpha})^{d_1}(\dot{\overline{\varepsilon}}^{in})^{d_2}$$

$$c = c'\left(\frac{L}{L_0}\right)^{m_5} \exp\left(-\frac{\Delta H(L)}{RT}\right) \quad [10]$$

Table III. Back-Stress Model and Corresponding Material Constants

$$\dot{S}^c_{ij} = \frac{2}{3}h_\alpha(\overline{\alpha}, L)\dot{\varepsilon}^{in}_{ij} - [r^D_\alpha(\overline{\alpha}, T, \dot{\overline{\varepsilon}}^{in}, L)\dot{\overline{\varepsilon}}^{in} + r^s_\alpha(\overline{\alpha}, T, L)]S^c_{ij}$$

$$h_\alpha(\alpha, L) = \begin{cases} a_1 \exp\{-[a_2(\alpha_0 + \overline{\alpha})]^{a3}\} & \text{if } \dot{\varepsilon}^{in} \cdot \alpha \geq 0 \\ a_1 \exp\{-[a_2(\alpha_0 - \overline{\alpha})]^{a3}\} & \text{if } \dot{\varepsilon}^{in} \cdot \alpha \leq 0 \end{cases}$$

$$a_1 = a_{10}\left(\frac{L}{L_0}\right)^{m2}, \; a_2 = a_{20}\left(\frac{L}{L_0}\right)^{m3}, \; a_3 = a_{30}\left(\frac{L}{L_0}\right)^{m4}$$

$$\dot{a}_i = -c_i(a_i - a_{i\text{sat}}) \exp\left(-\frac{\Delta H_i}{RT}\right) \quad (i = 1, 2, 3)$$

$$r^s_\alpha(\alpha, T, L) = 0$$

$$r^D_\alpha(\overline{\alpha}, T, \dot{\overline{\varepsilon}}^{in}, L) = c(\overline{\alpha})^{d1}(\dot{\overline{\varepsilon}}^{in})^{d2}$$

$$c = c'\left(\frac{L}{L_0}\right)^{m5} \exp\left[-\frac{\Delta H(L)}{RT}\right]$$

$$d_2 = d_{20}\left(\frac{L}{L_0}\right)^{m6}$$

$$\Delta H(L) = h_1 + h_2\left(\frac{L}{L_0}\right) + h_3\left(\frac{L}{L_0}\right)^2$$

$a_{10} = 8.0 \times 10^5$ MPa, $a_{20} = 1.1 \times 10^{-2}$/MPa, $a_{30} = 1.44$

$$\alpha_0 = 175 - 50\left(\frac{L}{L_0}\right)(\text{mpa})$$

$m_2 = -0.59$, $m_3 = 0.34$, $m_4 = -0.16$

$a_{1\text{sat}} = 1.8 \times 10^5$ MPa, $a_{2\text{sat}} = 0.10$/MPa, $a_{3\text{sat}} = 0.48$

$\Delta H_1 = 250.0$ kJ/mol, $\Delta H_2 = 180.0$ kJ/mol, $\Delta H_3 = 85.0$ kJ/mol

$c_1 = 9.3 \times 10^{18}$ s^{-1}, $c_2 = 3.6 \times 10^{11}$ s^{-1}, $c_3 = 3.9 \times 10^2$ s^{-1}

$c' = 4.8 \times 10^7$, $d_1 = -0.7$, $d_{20} = -0.23$

$m_5 = -6.6$, $m_6 = -0.37$

$h_1 = 87$ kJ/mol, $h_2 = -44$ kJ/mol, $h_3 = 4$ kJ/mol

$$d_2 = d_{20}\left(\frac{L}{L_0}\right)^{m_6}$$

where c', d_1, d_{20}, m_5, and m_6 are material constants. A summary of all constants is given in Table III.

C. *Hardening and Recovery Functions of Drag Stress*

The initial drag stress was determined by examining the monotonic inelastic strain-stress response. The evolution of the drag stress is determined by examining the cyclic material response. With measurements of the current yield-stress range ($2\overline{\sigma}$) and saturated yield-stress range ($2\overline{\sigma}_{\text{sat}}$), the corresponding levels of current drag stress and the value of drag stress at saturation (K_{sat}) can be determined by inverting Eq. [1] The saturated drag stress, as a function of temperature, was determined from the saturated response in a cyclic test at 250 °C with a frequency of 0.5 Hz and from RT tests with a strain rate of 5×10^{-3} s^{-1}.

The hardening function of drag stress (h_{kD}), which could produce cyclic hardening or softening to the stable state, can be expressed as

$$h_{kD}(K, T, L) = B(K_{\text{sat}} - K)\dot{\overline{\varepsilon}}^{in} \quad [11]$$

where B is the drag stress hardening-rate coefficient, and $\dot{\overline{\varepsilon}}^{in}$ is the effective inelastic strain rate. By rearranging the previous equation, it is possible to determine the drag stress hardening-rate coefficient directly from the experiment. The hardening-rate coefficient is the slope of the $\ln |K - K_{\text{sat}}|$

vs cumulative inelastic strain curve, as shown in Figure 7. The cyclic softening trends for both the small and large SDASs are similar. We note that K_{sat} is always lower than K_0, the initial value of drag stress, for these alloys.

In Eq. [11], the drag stress hardening-rate coefficient was usually regarded as a constant.[4,11,13] From Figure 7, it can be seen that the hardening-rate coefficient varies with the cumulative inelastic strain. Within the first several cycles, the variation of drag stress occurs at a higher rate than in later cycles. In this article, two values were selected for the hardening coefficient. At low cumulative inelastic strains or high values of $K - K_{sat}$, the value of B is large and, as $K - K_{sat}$ decreases, the value of B changes in bilinear fashion.

The drag stress recovery term (r_k) is important at high temperatures and low strain rates when hold periods are present. In order to determine the recovery term of drag stress, some specimens have been exposed to high temperatures under zero stress. The subsequent stress-strain response at RT was used to determine r_k (shown in Figure 11). The changes in drag stress for each test were measured to establish the drag stress recovery term. The r_k term is given as

$$r_k(K, T, L) = A_3\left(\frac{L}{L_o}\right)^{m7}(K - K_{rec}) \qquad [12]$$

$$A_3 = A_{30} \cdot \exp\left(-\frac{\Delta H_R}{RT}\right)$$

where A_3 is the drag stress recovery coefficient. The term $(L/L_0)_7^m$ describes the sensitivity to SDAS. The A_3 term simulates the rate at which K will tend to reach K_{rec}. The coefficient m_7 is near 1.5, which indicates that recovery occurs faster for materials with a large SDAS. The ΔH_R term represents the activation energy for the recovery process. The recovery term K_{rec} corresponds to the strength of the material after being subjected to a long thermal exposure. The meaning of the term K_{rec} was defined earlier (Sehitoglu[1]) by the following equation:

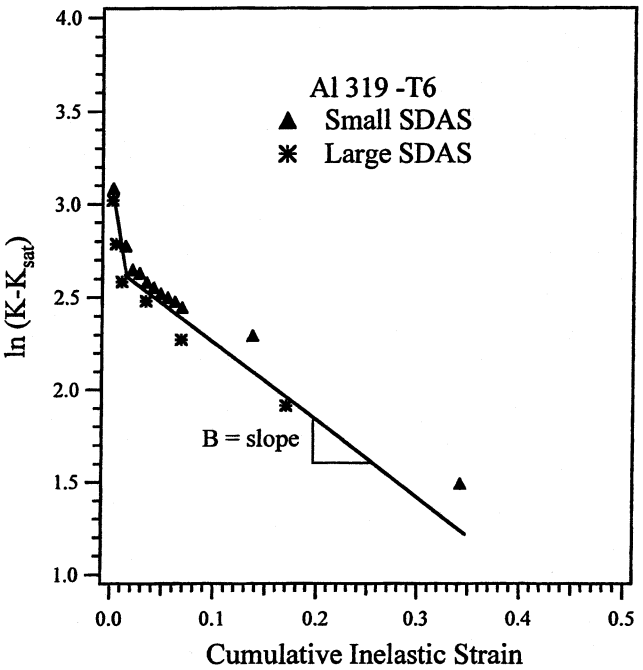

Fig. 7—Determination of drag stress hardening coefficient at 250 °C.

$$K_{rec} = K_o\left(\frac{\overline{\sigma}_{i+1}}{\overline{\sigma}_i}\right) + \int_t \theta\,\dot{T}\,dt \qquad [13]$$

where K_0 is the initial drag stress at the temperature of interest, and $\overline{\sigma}_{i+1}/\overline{\sigma}_i$ is the ratio of yield strength after recovery relative to the value before recovery. This ratio is determined by making yield-stress measurements (0.005 pct offset) on the samples. The values of A_3 and ΔH_R have been estimated from experiments after thermal exposure (Figure 11). The last item in Eq. [13] accounts for the effect of changing temperature on K_0, where $\theta = \partial K_0/\partial T_0$. The coefficients and constants are listed in Table IV.

As indicated earlier by Hasegawa *et al.*,[15] recovery behavior during thermal exposure is influenced by the application of external stresses. In the present study, inelastic deformation causes accelerated coarsening of precipitates. In Eq. [12], the drag-stress recovery coefficient A_3 should be a function of temperature and inelastic strain. To a first approximation, we assumed that A_3 is only a function of temperature, *i.e.*, A_{30} is a constant. We determined A_{30} from thermal-exposure experiments at zero load. The constant A_{30} was expressed as a function of (K-K_{rec}), as shown in Table IV, and its magnitude changed depending on whether the stress rate ($\overline{\sigma}/K$) is smaller or larger than 1. The satisfactory simulation shows that this representation is appropriate for the Al 319-T6A alloy.

To gain further insight into trends, a comparison of the K_0, K_{sat}, and K_{rec} levels to temperature, for cast a aluminum with a large SDAS, is shown in Figure 8. The K_0 curve is obtained by observing the inelastic deformation of virgin specimens. The K_{sat} curve in Figure 8 was obtained for cyclic experiments at high strain rates. The results demonstrate that the K_{rec} line lies substantially below the K_0 and K_{sat} curves. Note that Al 319-T6 alloys with different SDASs have the same K_{rec} value, but entirely different K_0 and K_{sat} values. This is an important observation because, in the limit of long exposure times, the results from different SDAS materials converge. As shown in Figure 8, K_{sat} and K_{rec} at RT are substantially different, because the drag stress decreased as

Table IV. Drag-Stress Model and Corresponding Material Constants

$K = h_k(K, T, L) - r_k(K, T, L) + \theta(K, T, L)T$
$h_{kD}(K, T, L,) = B(K_{sat} - K)\dot{\bar{\varepsilon}}^{in}$
$r_k(K, T, L) = A_3\left(\frac{L}{L_0}\right)^{m_7}(K - K_{rec})$
$A_3 = A_{30}\exp\left[-\frac{\Delta H_R}{RT}\right]$
$K_{sat} = k_{sat1}\left(\frac{L}{L_0}\right)^{m_8} - k_{sat2}\left(\frac{L}{L_0}\right)^{m_9} T\ (°C)$
$K_{rec} = 25.0$ MPa, when $T = 250$ °C
$B = 26$, if $K - K_{sat} \geq 13$ MPa
$B = 6$, if $K - K_{sat} < 13$ MPa
$A_{30} = 6.0 \times 10^6\ s^{-1}$, if $\frac{\overline{\sigma}}{K} < 1$
$A_{30} = 1.2 \times 10^5(K - K_{rec})^{1.7}\ s^{-1}$, if $\frac{\overline{\sigma}}{K} \leq 1$
$\Delta H_R = 121.0$ KJ/mol, $m_7 = 1.47$
$k_{sat1} = 108.2$ MPa, $k_{sat2} = 0.160$ MPa/°C
$m_8 = -0.25$ $m_9 = -0.50$

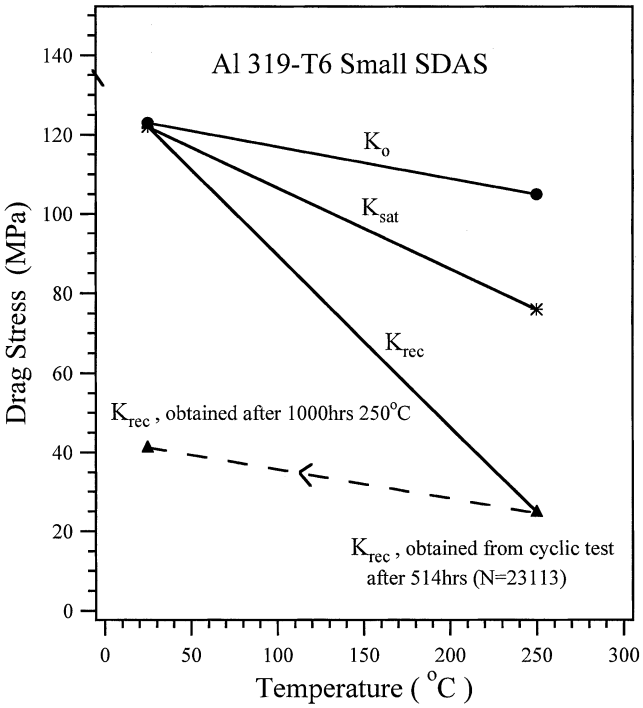

Fig. 8—The changes of drag stress (K_o, K_{ast}, and K_{rec}) with temperature.

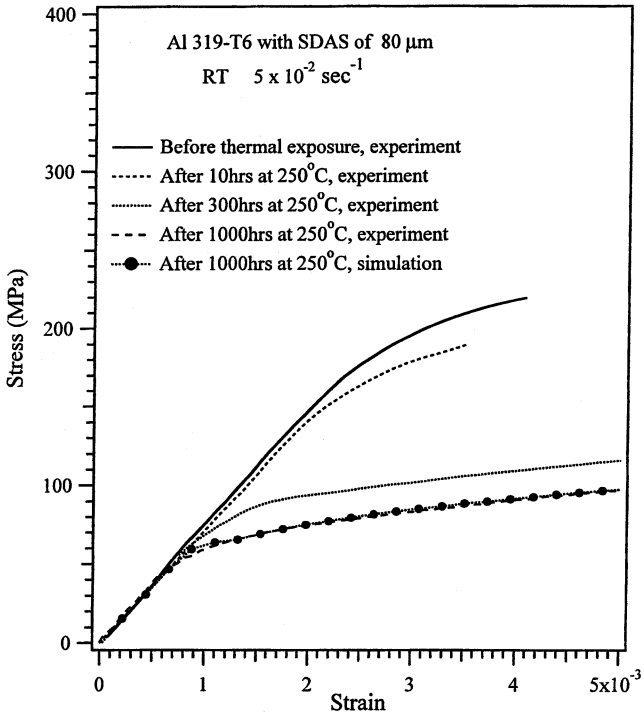

Fig. 9—Stress-strain response of Al 319-T6 with SDAS of 80 μm before and after thermal exposure.

a result of either cyclic deformation or long-term exposure to high temperatures.

The K_{rec} curve is obtained as follows: If the material is subjected to cyclic loading at 250 °C after many hours (>500 hours) the K value approaches 25 MPa. Alternatively, if the specimen was thermally exposed at 250 °C for 1000 hours then tested at 25 °C, the K_{rec} value at RT is 40 MPa. Both data points are shown in Figure 8 and are entirely consistent, because the difference between the two results is the $\int_t \theta T dt$ term. The dashed line (with same slope, $-K_2(L/L_0)^{m_1}$, as the K_0 line) in Figure 8 is the hypothetical line, which could be used to determine the RT strength of the material after long-term exposure to a temperature of 250 °C. For exposure to other temperatures, follow the K_{rec} curve and draw a similar dashed line.

IV. COMPARISONS OF MODEL SIMULATIONS TO EXPERIMENTS

The capabilities of the constitutive model outlined previously are checked against a variety of experiments in this section. In order to determine the variation of drag stress and back-stress after thermal exposure at high temperatures, a series of monotonic tensile tests on the Al 319-T6 alloy with a SDAS of 80 μm were performed at RT, after the materials had been exposed to 250 °C and 180 °C at zero load. The experimental results and simulation of the monotonic stress-strain response at RT, after the material had been thermally exposed at 250 °C for 1000 hours, are given in Figure 9. We note that the strength and strain-hardening rate decreased considerably upon high-temperature exposure. The predictions (solid points) are shown only for the 1000-hour-exposure case, but the experimental results for 10 and 300 hours of exposure are also shown for comparison.

Simulations of the stress-strain response for Al 319-T6 alloy samples with small and large SDASs during isothermal fatigue at high temperatures (low strain rates), and the corresponding experiments, shown in Figures 10 and 11. We note that the model simulates the cyclic softening behavior, hysteresis loop shapes, and forward and reverse yielding points very accurately. To check the capabilities of the model and to predict stress-strain behavior at different strain rates, comparisons between the simulation and experiment, using an Al 319-T6 alloy with a small SDAS under isothermal fatigue (at 0.5 Hz), are presented in Figure 12. The stress levels are substantially higher in this case, and the degree of softening

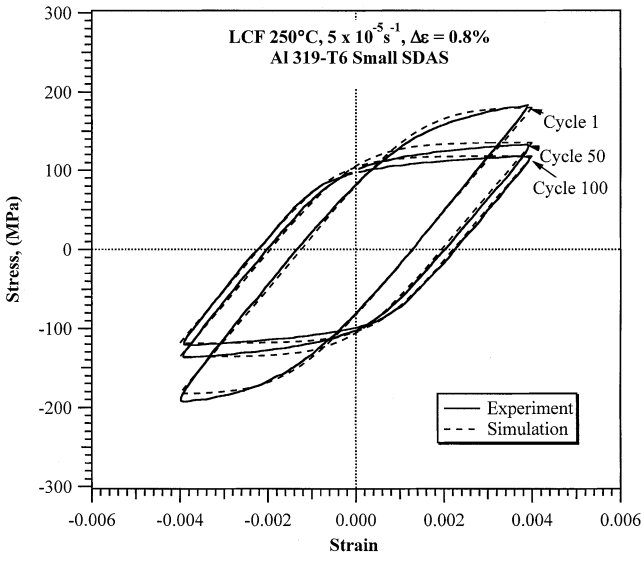

Fig. 10—Isothermal cyclic stress-strain behavior of Al 319-T6 small SDAS at 250 °C, a strain rate of 5×10^{-5} s^{-1}, and a strain range of 0.8 pct.

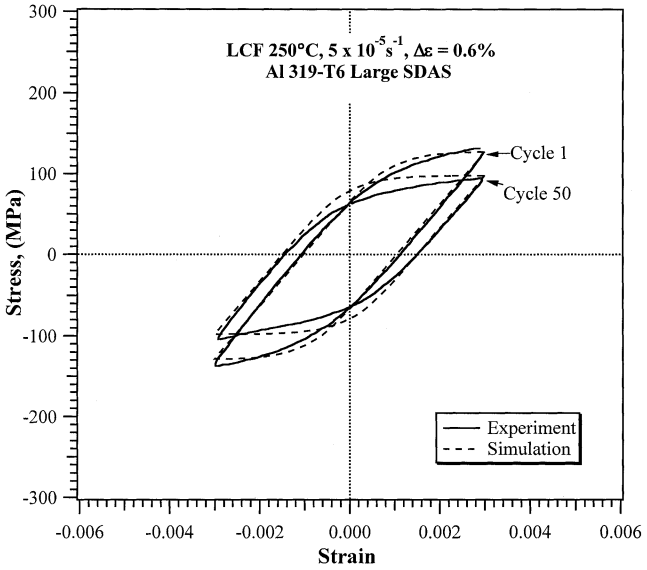

Fig. 11—Isothermal cyclic stress-strain behavior of Al 319-T6 large SDAS at 250 °C, a strain rate of 5×10^{-5} s^{-1} and a strain range of 0.6. pct.

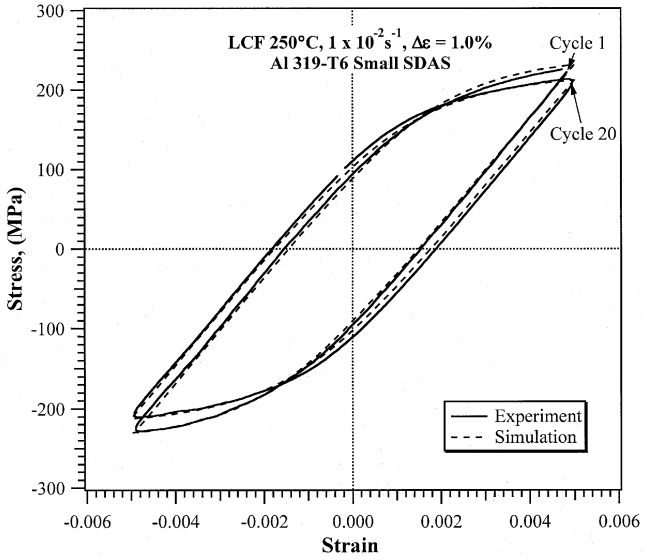

Fig. 12—Isothermal cyclic stress-strain behavior of Al 319-T6 small SDAS at 250 °C, a strain rate of 1×10^{-2} s^{-1}, and a strain range of 1.0 pct.

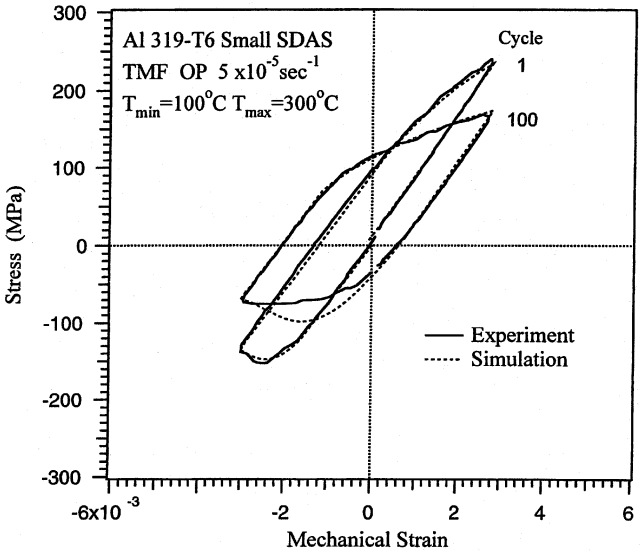

Fig. 13—Comparison of experiment and simulation for TMF OP stress-strain behavior of Al 319-T6 small SDAS.

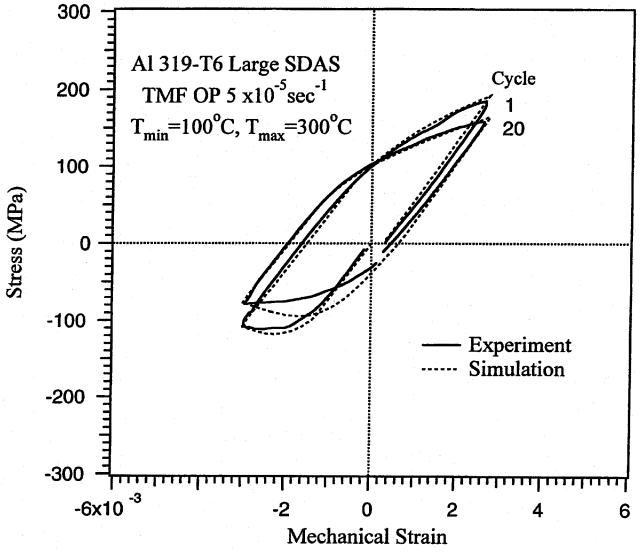

Fig. 14—Comparison of experiment and simulation for TMF OP stress-strain behavior of Al 319-T6 large SDAS.

is small. Nevertheless, the model predicts the cyclic softening behavior and the plastic-strain range in cycles very satisfactorily.

The constitutive model was checked with independent TMF loading experiments. The typical hysteresis loops of the TMF (OP) experiment for a small SDAS, for a strain range of 0.6 pct, is given in Figure 13. The loops are shown for cycles 1 and 100. Considerable softening occurs with cycles during the TMF OP experiment. The experimental results are denoted by the solid line, and the predictions are shown with dashed lines. We note that the model predicts the maximum stress levels, minimum stress levels, and the inelastic strain range in the cycle extremely well.

The TMF OP behavior for a material with a large SDAS is shown in Figure 14. In this case, cycles 1 and 20 are shown (the lifetime is shorter than that for a small SDAS), and the simulations are in agreement with the experiments. We note that the stress levels in tension and in compression are lower for the material with a large SDAS than for the one with a small SDAS. Finally, a comparison of simulation and experiment for the Al 319-T6 alloy with a medium SDAS under a TMF OP condition is given in Figure 15. This case represents a critical check of the predictive capabilities of the unified constitutive model, because the material with a medium SDAS was not used to establish the constants. Note that the stress levels in the case of a medium SDAS are predicted accurately, and the stress levels are much closer to those for a material with a small SDAS than for that with a large SDAS.

The results show clearly that the drag stress and back-stress hardening term decreased substantially after the material had been exposed to high temperatures. Numerous

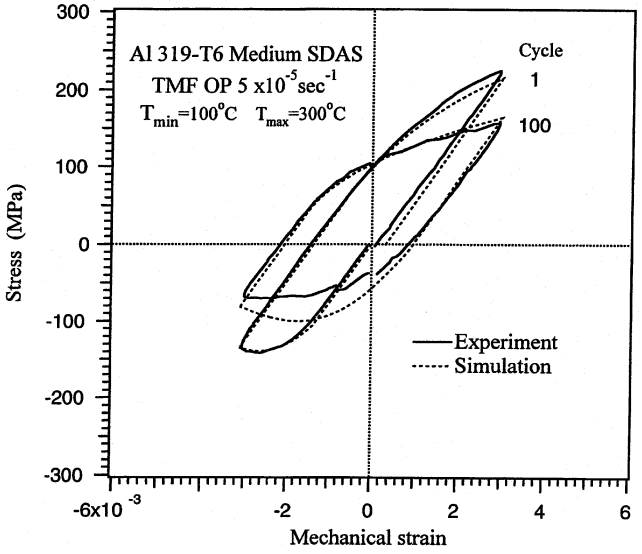

Fig. 15—Comparison of experiment and simulation for TMF OP stress-strain behavior of Al 319-T6 medium SDAS.

experimental results and simulations (dashed line) obtained from exposure to various temperatures and subsequent testing at RT are summarized in Figure 16.[21] The vertical axis is the yield strength, and the horizontal axis is the exposure time. We note that the majority of the microstructurally induced changes occur upon exposure to temperatures above 180 °C. The results show that the decrease in strength levels is as high as a factor of 2.5. Such a large change in mechanical behavior corresponds to drastic microstructural changes.

V. MICROSTRUCTURAL OBSERVATIONS

As mentioned earlier, the materials considered in this article underwent a T6 heat treatment (8 h/495 °C/water quenching + 5 h/190 °C) to achieve a peak-aged condition.

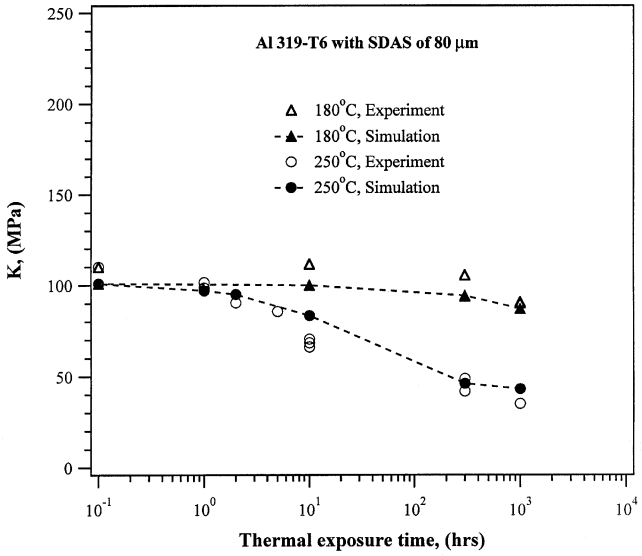

Fig. 16—Relation between drag stress in RT and thermal exposure time at 180 °C and 250 °C ($\sigma' y/K = 1.32$).

When the specimens were exposed to high temperatures, the precipitates underwent additional aging and the strength decreased due to overaging. The driving force is such that dissolution of small particles to the matrix occurs while the large precipitates grow. Both phenomena resulted in an increase in distance between obstacles as the thermal exposure progressed. To gain further insight into the results, a TEM study was undertaken. The TEM microstructure of the undeformed material and of the same material after thermal exposure at 250 °C for 1000 hours are shown in Figures 17(a) and (b), respectively. Comparing Figures 17(a) and (b), the amount of microstructural coarsening is visible. Note the formation of regions that are nearly free of precipitates, as well as the presence of large precipitates, in Figure 17(b).

The decrease of flow stress resulting from thermal exposure has been considered in the constitutive model as well as the variation of the back-stress hardening term (*via* Eqs. [12] and [10], respectively). The change in the back-stress

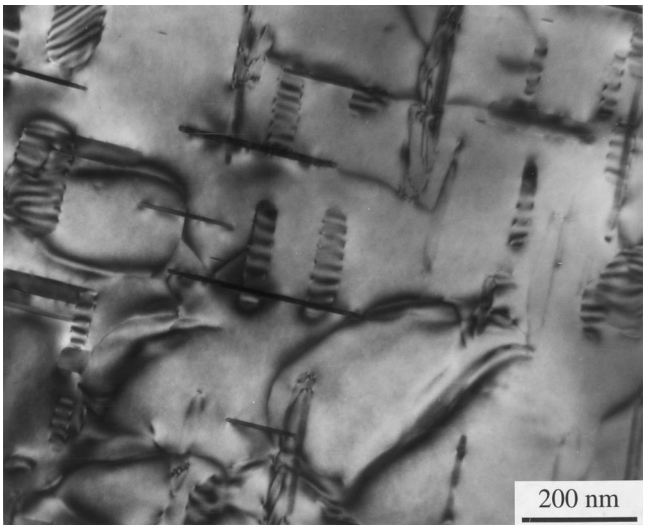

(*a*)

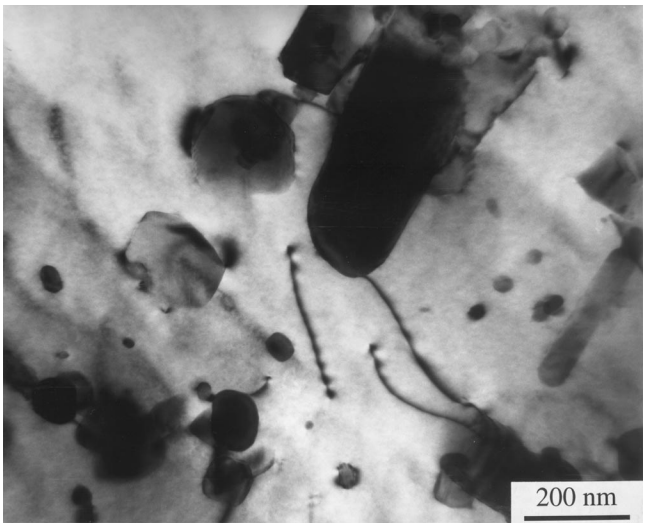

(*b*)

Fig. 17—Two-beam TEM bright-field images showing (*a*) undeformed materials and (*b*) coarse microstructure obtained after 1000 h at 250 °C.

hardening rate is considerable, as observed in the experiments. This change was considered *via* the time evolution of the constant a_i, in addition to the flow-stress decrease to capture the material response.

A PHILIPS XL30 scanning electron microscope with a motorized stage and a conventional energy-dispersive X-ray spectrometer was used to quantify the primary $CuAl_2$ segregates. For the specimens a medium SDAS, a total of 4183 randomly distributed spots were analyzed and the average volume fraction of primary $CuAl_2$ segregates was determined. Each spot was analyzed for 20 seconds at 20 kV, and a few thousand data points were obtained to develop a sufficient amount of data. From this, the average copper content in the aluminum matrix was calculated to be 2.59 pct for a large SDAS, 2.84 pct for a medium SDAS, and 3.41 pct for a small SDAS. Note that experiments show that cast aluminum 319-T6 with different SDASs has almost the same stress-strain response after long-term exposure to high temperatures. This confirms that, after long exposures, the θ' precipitates within the dendrites (not the primary $CuAl_2$) coarsen and dissolve into the matrix, resulting in a microstructure independent of the initial SDAS.

The maximum volume fraction that can be precipitated was calculated[16] using the Al-Cu phase diagram, the copper content soluble in the matrix, the average copper content in the matrix, the volume of unit cell of theta prime, the copper content in solution (given previously), and the number of atoms in a unit cell of theta prime. It was determined that the small SDAS has nearly a 4.0 pct volume fraction of theta prime precipitates, while the large SDAS has nearly 3.0 pct. This indicates a large difference in volume fraction between the small and large SDASs, as is obvious from the stress-strain data. Note that these numbers should be considered very approximate. For accurate measurements of volume fractions of theta prime, one has to optimize the TEM foils and look at many samples to develop statistical significance. This is beyond the scope of this article.

VI. DISCUSSION OF RESULTS

It is clearly seen that the stress-strain response of cast aluminum alloys is strongly dependent on SDAS, *i.e.*, the initial microstructure. The yield strength and hardening rate increases as the SDAS becomes finer. The material with a small SDAS displayed a higher initial drag stress and higher strain-hardening rate than the material with a large SDAS. As mentioned earlier,[7,17,18] the SDAS was directly influenced by the solidification rate of the metal. Rapid solidification in castings not only produces a finer SDAS, but also supresses and refines the $CuAl_2$ eutectic which forms (typically at grain boundaries) during solidification. After solution tretament and aging, a fine, uniform precipitate structure forms. In the coarse structures obtained when the cooling rate is relatively slow, the $CuAl_2$ segregate content is higher, thus depleting the Cu content from the dendritic regions.[19,20] As a result, the postaging θ' precipitate, which produces the primary strengthening structure, is not as evenly distributed or as fine as in the case of a small SDAS.

It is very difficult to predict the constants in the unified model from micromechanical theories. The stress exponents in the plasticity and power-law creep regimes are 6 and 13, respectively. It has been very common to find exponents as high as 20 in precipitation-hardened alloys. These exponents do not change, even if the threshold stress is subtracted from the stress and an effective stress is defined. Weertman[22] has discussed extensively the deviation of the power-law creep exponent from 3 at high stresses and attributed the higher exponents to the stress dependence of the glide portion of the dislocation motion. Accounting for the glide portion of dislocation motion in the power-law creep regime, an exponent near 6 is reasonable. Further studies are needed to amplify these issues.

The other term of interest in our constitutive model is the back-stress hardening rate. In early works, a number of models have emerged for determining the strain-hardening behavior based on the geometric slip distance. If dislocation pileup occurs over a length comparable to the precipitate spacing, the back-stress hardening rate should increase as the spacing between the precipitates is reduced.[23] Models based on dislocation bowing between precipitates, accounting for local stresses, also predict a dependence of the hardening behavior (Brown and Stobbs[24]) on the spacing between the precipitates. Similarly, the "geometrically necessary dislocations" concept of Reference 25 predicts that the strain-hardening rate (in the absence of recovery) depends on the distance between particles. Our experimental results show that the hardening rate, to a first approximation, varies as $L^{-0.5}$, where L is the SDAS (m_2 was found to be near -0.5 (Table III)). Although the exact relationship between L and the precipitate spacing is not known, the finer SDASs produce higher Cu contents in solution (Section V), which, in turn, results in a higher volume fraction of θ' and a smaller distance between precipitates. Both solid-solution and precipitation-hardening contributions are present in these alloys and, at the moment, the magnitude of the back-stress hardening term dependency on L is established directly from experiments. Determining the exact derivation of this dependency based on microstructural parameters is beyond the scope of this article.

We also note that the dynamic recovery term in the back-stress expression is dependent on the length parameter. Our results show (Table III) that the recovery term is higher for the material with a small SDAS and increases with higher temperatures. The increased recovery rate with smaller-size incoherent precipitates has been explained by Ashby[25] by the smaller diffusion distance or shorter high-diffusivity paths during climb of dislocations around particles. Since we expect that the precipitate size and spacing is influenced by the solidification rate (which, in parallel, affects the SDAS length) the results obtained in the present study are consistent with the simple models of recovery.

Another observation can be made on the dependence of the flow rule on the length parameter (Table III). In our work, we found that the inelastic strain rate increases with the length parameter as L^2, *i.e.*, the higher the dendrite arm spacing, the higher the inelastic strain rate. This dependence is in qualitative agreement with the work of Shewfelt and Brown,[26] who analyzed creep *via* dislocation climb over nondeforming obstacles. Both of these works predict that the inelastic flow rate increases with the increasing "characteristic" length, which is the distance between the barriers opposing dislocation flow. These models are useful, but, at

*PHILIPS is a trademark of Philips Eletronic Instruments Corp., Mahwah, NJ.

this time, we still need to rely on the phenomenological model as proposed here to predict stress-strain response under complex loading conditions.[27]

The unified model provided a successful simulation for cyclic stress-strain curves, material behavior after thermal exposure, and material response under thermomechanical deformations at high temperatures. The simulation of the material stress-strain response under thermomechanical loading provided a critical check of the capabilities of the constitutive model. The temperature and strain histories studied are rather complex, and these experiments were not used to establish the constitutive model. It can be seen in Figures 13 through 15 that the stress-strain response at both the low-temperature and high-temperature end of the cycle were accurately predicted.

VII. CONCLUSIONS

This work supports the following conclusions.

1. A two state–variable unified constitutive model proposed earlier by the author was modified to describe the stress-strain response of a Al 319-T6 alloy with different SDASs. Model predictions of the stress-strain response under a wide variety of temperature and strain conditions were compared to experiments, and accurate predictions were achieved consistently.
2. The cyclic stress-strain response depends strongly on solidification conditions. The flow rule and the initial value of drag stress are considerably influenced by the length of the SDAS. The material constants depend on the solidification rate (as characterized by the SDAS length) in a nonlinear fashion. In all cases, the rapidly solidified material with a small SDAS (<30 μm) displayed the highest cyclic stress-strain amplitudes, with the stress levels decreasing gradually as the SDAS levels approach 100 μm. We found, as expected, that the copper content in solution decreased as the SDAS increased, and this explains the softer response of microstructures with a large SDAS. After long-term high-temperature exposure, the α-ε responses of the extreme microstructures converged.
3. Due to the significant coarsening of the material microstructure resulting from thermal exposure at 180°C and 250 °C for nearly 1000 hours, the recovery of drag stress was considered in the constitutive model as well as the variation of back-stress. For Al 319-T6, the fully recovered value of drag stress is considerably smaller than the initial drag stress values, by a factor of 2.5 in some cases. The slope of the stress–inelastic strain curve also decreased, by tenfold under extreme conditions. The functions in the constitutive model were systematically established from experiments upon measuring the decrease in yield strength (drag stress) and strain-hardening behavior (back-stress).
4. The cyclic softening of drag stress in the first several cycles was much more rapid at high stresses. As the stress levels decreased, the rate of softening also decreased, and this was predicted accurately with the model. Experiments which were not used to derive the model include TMF experiments, where the temperature was cycled from 100 °C to 300 °C, and experiments employing cyclic loading of materials with a medium SDA: The accuracy of the prediction was remarkable for all these cases, considering the complexity of the deformation in these alloys.
5. The proposed model is capable of simulating the transition from the initial to final drag stress as a function of temperature and time. The results of the model were supported by TEM of samples thermally exposed at 250 °C. The micrographs showed that the precipitates approached a spherical shape in the limit, and the spacing between the precipitates increased considerably. The micromechanical models proposed to capture these trends are at an infancy stage, and phenomenological models with cognizance of microstructural features represent a positive step in stress-strain prediction.

ACKNOWLEDGMENTS

This work is supported by Ford Motor Company. Paula Reeber is thanked for providing her unpublished thermal exposure results. Mr. John Lasecki, Ford, assisted with the preparation of the material and a portion of the isothermal test program at Westmoreland and Metcut. The TEM investigations were completed at the Center for Micro Analysis of Materials at the University of Illinois funded by the Department of Energy under Grant No. DEFG 02 91-ER45439.

REFERENCES

1. H. Sehitoglu: *ASME J. Eng. Mater. Technol.* 1989, vol. 111, pp. 192-203.
2. D.C. Slavik and H. Sehitoglu: in *Thermal Stress, Material Deformation, and Thermo-Mechanical Fatigue*, [ASME PVP 123,] H. Sehitoglu and S.Y. Zamrik, eds., ASME, Fairfield, NI,
3. D.C. Slavik and H. Sehitoglu: in *Thermal Stress, Material Deformation, and Thermo-Mechanical Fatigue*, [ASME PVP 123,] H. Sehitoglu and S.Y. Zamrik, eds., ASME, Fairfield, NI, 1987, pp. 65-74.
4. H. Sehitoglu: *Handbook on Fatigue and Fracture*, ASM, Materials Park, OH, 1996, vol. 19, pp. 527-54.
5. J.A. Eady and D.M. Smith: *SAE Trans.* 1984, vol. 93, pp. 747-55.
6. J.B. Andrews, and M.V.C. Seneviratne: *Trans. AFMS*, 1984, vol. 92, pp. 209-16.
7. R.B. Gundlach, B. Ross, A. Hetke, S. Valtierra and J.F. Mojica: *AFS Trans.*, 1994, vol. 102, pp. 205-23.
8. H.R. Shercliff and M.F. Ashby: *Acta Metall. Mater.*, 1990, vol. 38 (10), pp. 1789-1802.
9. D.C. Drucker and L. Palgen: *ASME J. Appl. Mech.*, 1981, vol. 48, pp. 479-85.
10. Y. Jiang and H. Sehitoglu: *J. Appl. Mech.*, 1996, vol. 63, pp. 726-33.
11. H. Sehitoglu: in *NATO ASI—Mechanical Behavior of Materials at High Temperature*, C. Moura Branco, R. Ritchie, and V. Sklenicka, eds., Kluwer, Hingham, MA, 1996, pp. 349-79.
12. S.R. Bodner and Y. Partom: *ASME J. Appl. Mech.* 1975, vol. 42, pp. 385-89.
13. M. Karayaka and H. Sehitoglu: in *Fracture, and Nondestructive Evaluation of Advanced Materials*, ASTM STP 1157, M.R. Mitchell and O. Buck, eds., A9STM, Philadelphia, PA, 1992, pp. 101-20.
14. J. Boileau, P. Collins, and J.E. Allison: *Proc. 5th Int. AFS Conf. on Molten Aluminum Processing*, AFS Inc. Des Plaines, IL, 1998, pp. 157-72.
15. T. Hasegawa, T. Yakou, and U.F. Kocks: *Acta Metall.*, 1982, vol. 30, pp. 235-43.
16. M.V. Heimendahl and G. Wassermann: *Z. Metallkde.*, 1962, vol. 53, pp. 275-83.
17. M.C. Flemings, T.Z. Kattamis, and B.P. Bardes: *AFS Trans.* 1991, vol. 99, pp. 501-06.
18. A. Hetke and R.B. Gundlach: *AFS Trans.* 1994, vol. 102, pp. 367-80.
19. M.C. Flemings: *Prem. Qual. Al. Castings*, 1963, July pp. 60-63.
20. M.C. Flemings, S.Z. Uram, and H.F. Taylor: *AFS Trans.* 1960 vol. 68, pp. 670-84.
21. P. Reeber: Ford Research Laboratory, Dearborn, MI, Private Communication, 1998.

22. J. Weertman: *J. Appl. Phys.* 1957, vol. 28, p. 362.
23. K. Tanaka and T. Mura: *ASME J. Appl. Mech.* 1981, vol. 48, pp. 97-103.
24. L.M. Brown and W.M. Stobbs: *Phil. Mag.* 1971, vol. 23, pp. 1185-99.
25. M.E. Ashby: in *Strengthening Methods in Crystals*, A. Kelly and R.B. Nicholson, eds. Elsevier, Amsterdam, 1971, p. 137.
26. R.S.W. Shewfelt and L.M. Brown: *Phil. Mag.* vol. 35, 1977, pp. 945-62.
27. T.J. Smith, H.J. Maier, H. Sehitoglu, and E. Fleury and J. Allison: *Metall. Mater. Trans. A*, 1999, vol. 30A, pp. 133-46.